Letter

Temperature-dependent band modification and energy dependence of the electron-phonon interaction in the topological surface state on Bi_2Te_3

Amit Kumar [1,*] Shiv Kumar [1,2,3,†] Yudai Miyai,[2] and Kenya Shimada [1,2,3,‡]

[1]*Department of Physical Science, Graduate School of Science, Hiroshima University, Kagamiyama 1-3-1, Higashi-Hiroshima 739-8526, Japan*

[2]*Physics Program, Graduate School of Advanced Science and Engineering, Hiroshima University, Kagamiyama 1-3-1, Higashi-Hiroshima 739-8526, Japan*

[3]*Hiroshima Synchrotron Radiation Center, Hiroshima University, Kagamiyama 2-313, Higashi-Hiroshima 739-0046, Japan*

(Received 22 May 2022; revised 21 July 2022; accepted 12 August 2022; published 12 September 2022)

We report the temperature-dependent band structure and energy dependence of the electron-phonon interaction of the topological surface state (TSS) on the three-dimensional topological insulator Bi_2Te_3 using angle-resolved photoemission spectroscopy. Despite the nonrigid-band-like band modification as the temperature increases, the degeneracy at the Dirac point (DP) was robust, indicating topological protection. The electron-phonon coupling parameter depends on the initial-state electron energy, varying from 0.13 (at the DP) to 0.02 (100 meV above the DP), in agreement with reported first-principles calculations. Our findings provide insight into the physical properties derived from TSSs at finite temperatures.

DOI: 10.1103/PhysRevB.106.L121104

A three-dimensional (3D) topological insulator (TI), which is a quantum state of matter under strong spin-orbit coupling (SOC) and time-reversal symmetry, has attracted much interest in the past decade [1–5]. Metallic topological surface states (TSSs) inside the bulk band gap of 3D TIs degenerate at the time-reversal invariant momentum (TRIM) and exhibit a Dirac-fermion-like linear dispersion away from the TRIM [2,3]. The electron spin and momentum directions of the TSS are mutually locked due to the strong SOC, yielding a peculiar helical spin texture in momentum space [6]. The helical spin texture of the TSS suppresses backscattering due to lattice defects or nonmagnetic impurities [7], leading to a prolonged quasiparticle lifetime and enhanced electrical conductivity and mobility. Furthermore, the metallic nature of the TSS is robust under perturbations that conserve the Z_2 topological invariants [3–5]. Three-dimensional TIs have attracted much interest not only for their intriguing physical properties, such as the quantum spin Hall effect [8], quantum anomalous Hall effect [9], Majorana fermions in the superconducting state [10,11], and magnetic monopole [12], but also for their potential spintronic applications [13].

Physical properties are closely related to quasiparticle properties at finite temperature, which can be formulated by using a single-particle thermal Green's function, which includes a self-energy (Σ) incorporating many-body interactions such as the electron-phonon interaction (EPI) and electron-electron interaction [14–16]. The imaginary part of the self-energy ($\mathrm{Im}\Sigma$) is directly related to the reciprocal of the relaxation time ($1/\tau$) at a given electron momentum and energy, and the average relaxation time at the Fermi surface is proportional to the electrical conductivity and mobility, which are essential parameters for electronic applications. The EPI, in particular, plays a significant role in the transport properties at finite temperature [15,16], the temperature-dependent reduction of the band gap [17,18], the temperature-induced topological phase transition [19], and the enhanced thermoelectric properties [20]. To clarify the superconductivity of Bi_2Se_3 observed upon Cu [11], Sr [21], and Nb [22] intercalation, the role of the EPI should also be characterized.

To date, intensive efforts have been applied to revealing the EPI in the TSSs of prototypical 3D TIs, Bi_2Se_3 and Bi_2Te_3 [23–41]. Despite the expected suppression of back scattering in the TSS [7], the transport measurements on Bi_2Se_3 suggested signatures of scattering due to the EPI [23,24]. To directly probe the surface phonons on Bi_2Se_3 and Bi_2Te_3, helium atom scattering (HAS) measurements have been performed [25–30]. For Bi_2Te_3, HAS measurements indicated that the EPI coupling parameter was in the range $\lambda_{ep} = 0.04-0.11$ and depended on the carrier concentration [30].

High-resolution angle-resolved photoemission spectroscopy (ARPES) is a powerful tool for investigating quasiparticle properties because the ARPES spectrum corresponds to the imaginary part of the single-particle Green's function [42–44]. Temperature-dependent high-resolution ARPES measurements revealed EPI coupling parameters of $\lambda_{ep} \sim 0.25$ [31] and $\lambda_{ep} \sim 0.076-0.088$ [32] for Bi_2Se_3 and $\lambda_{ep} \sim 0.17$ [33] for Bi_2Te_3. High-resolution ARPES measurements further revealed a kink structure due to the EPI in the energy band dispersion of the TSS near the Fermi level (E_F) at low temperature [34,35]. Kondo *et al.* [34] observed an extremely large coupling parameter of $\lambda_{ep} \sim 3$, which was discussed from the viewpoint of coupling to spin plasmons [45] and the Kohn anomaly of the surface

*amitk-physics19@hiroshima-u.ac.jp
†shivphy@hiroshima-u.ac.jp
‡kshimada@hiroshima-u.ac.jp

phonon mode [25]. On the other hand, Chen *et al.* found that the coupling parameters were $\lambda_{ep} \sim 0.17$ for Bi_2Se_3 and $\lambda_{ep} \sim 0.19$ for *n*-type Bi_2Te_3 [35]. They also found that the EPI coupling parameter depended on the E_F position, from $\lambda_{ep} \sim 0$ (*p*-type Bi_2Te_3) up to 0.19 (*n*-type Bi_2Te_3) [35]. Recent extensive first-principles calculations indicated that the EPI coupling parameters were $\lambda_{ep} < 0.3$ for Bi_2Se_3 and $\lambda_{ep} < 0.15$ for Bi_2Te_3, and the value of λ_{ep} varied depending on the initial-state electron energy [41].

Despite the significance of the initial-state electron energy dependence of the EPI coupling parameter in the TSS, there has not been a systematic study on this issue. Clarifying the determining factor of the magnitude of the EPI and its influence on the quasiparticle properties such as the lifetime is also required. In this study, therefore, we performed temperature-dependent high-resolution ARPES measurements on *n*-type Bi_2Te_3 single crystals. We have revealed temperature-dependent nonrigid-band-like band modification and the magnitudes of the EPI coupling parameter as a function of the initial-state electron energy. Our findings provide insight into the doping and temperature dependence of the transport properties derived from the TSS on 3D TIs.

First, we briefly summarize two methods to determine the EPI coupling parameter based on the ARPES line-shape analyses. One method is to analyze the kink structure or reduction in the group velocity due to the EPI near the E_F at low temperature. The group velocity of the energy band is reduced by a factor of $1/(1+\lambda_{ep})$, where λ_{ep} is the EPI coupling parameter [34,35]. At finite temperatures, the coupling parameter due to the EPI is defined as

$$\lambda_{ep}(\vec{k}_F, \omega = 0; T) = -\frac{\partial \mathrm{Re}\Sigma_{ep}(\vec{k}, \omega; T)}{\partial \omega}\Big|_{\omega=0},$$

where $\mathrm{Re}\Sigma_{ep}(\vec{k}, \omega; T)$ is the real part of the self-energy due to the EPI [15]. Via the temperature dependence of $\Sigma_{ep}(\vec{k}, \omega; T)$, the magnitude of the kink structure decreases as the temperature increases [15,27,46].

The other method is to use the slope of the temperature dependence of the imaginary part of the self-energy $|\mathrm{Im}\Sigma_{ep}(\vec{k}, \omega; T)|$ at the initial-state electron energy ω measured from E_F with a momentum $\vec{k}$ [31–33,43,44]. The ARPES linewidth due to the EPI at $\vec{k}$ and ω is given by

$$\begin{aligned}\Gamma_{ep}(\vec{k}, \omega; T) &= 2|\mathrm{Im}\Sigma_{ep}(\vec{k}, \omega; T)| \\ &= 2\pi \int_0^{\omega_D} d\tilde{\omega}\alpha^2F(\vec{k}, \omega; \tilde{\omega})[f(\tilde{\omega}+\omega, T) \\ &\quad + f(\tilde{\omega}-\omega, T) + 2n(\tilde{\omega}, T)],\end{aligned}$$

where $n(\omega, T)$ is the Bose-Einstein function, $f(\omega, T)$ is the Fermi-Dirac distribution function, and ω_D is the Debye energy [15,44]. The function $\alpha^2F(\vec{k}, \omega; \tilde{\omega})$ is defined by

$$\begin{aligned}\alpha^2F(\vec{k}, \omega; \tilde{\omega}) &= \sum_f \delta(\omega - \omega_f \pm \tilde{\omega}) \\ &\quad \times \sum_{\vec{q},\nu} |g^{i,f}(\vec{k}; \vec{q}, \nu)|^2 \delta(\tilde{\omega} - \omega_{\vec{q},\nu}),\end{aligned}$$

where $\vec{q}$ and ν represent the phonon momentum and phonon mode index, respectively; $\omega_{\vec{q},\nu}$ is the energy of the phonon with $\vec{q}$ and ν; and $g^{i,f}(\vec{k}; \vec{q}, \nu)$ is the matrix element of the electron-phonon scattering from the initial-state electron with $\vec{k}$ and ω to the final-state electron with $\vec{k}+\vec{q}$ and ω_f [41,44]. At elevated temperatures, $k_BT > \omega_D$, the temperature dependence of the linewidth can be approximated by

$$\Gamma_{ep}(\vec{k}, \omega; T) \sim C - 2\pi\lambda_{ep}(\vec{k}, \omega)k_BT,$$

where $C = 2\pi \int_0^{\omega_D} \alpha^2F(\vec{k}, \omega; \tilde{\omega})d\tilde{\omega}$ is a constant (temperature independent), and

$$\lambda_{ep}(\vec{k}, \omega) = 2\int_0^{\omega_D} \frac{\alpha^2F(\vec{k}, \omega; \tilde{\omega})}{\tilde{\omega}} d\tilde{\omega}$$

is the EPI coupling parameter at zero temperature at the fixed initial electronic state with $\vec{k}$ and ω. Therefore, the EPI coupling parameter $\lambda_{ep}(\vec{k}, \omega)$ can be calculated from the slope of the temperature-dependent ARPES linewidth $\Gamma_{ep}(\vec{k}, \omega; T)$. When the electron-phonon matrix element depends weakly on the initial-state electron energy and the electron-phonon scattering can be regarded as nearly elastic, namely, $\omega \sim \omega_f$, assuming that $|\tilde{\omega}/\omega| \leqslant |\omega_D/\omega| \ll 1$, we may have the relation

$$\alpha^2F(\vec{k}, \omega; \tilde{\omega}) \sim D(\omega) \sum_{\vec{q},\nu} |g^{i,f}(\vec{k}; \vec{q}, \nu)|^2 \delta(\tilde{\omega} - \omega_{\vec{q},\nu}),$$

where $D(\omega) = \sum_f \delta(\omega - \omega_f)$ is the density of states (DOS) at ω. In this case, the magnitudes of $\alpha^2F(\vec{k}, \omega; \tilde{\omega})$ and $\lambda_{ep}(\vec{k}, \omega)$ are proportional to $D(\omega)$ [41,44], which is indeed what we observe in this study.

High-quality *n*-type Bi_2Te_3 single crystals were grown by a direct melt reaction method [47,48], as detailed in the Supplemental Material [49]. The *n*-type sample is suitable in this study because we can detect the conduction band (CB) and evaluate the energy gap in the bulk. High-resolution ARPES measurements were performed using a μ-ARPES system equipped with a high-resolution electron-energy analyzer (VG Scienta R4000) and a focused ultraviolet laser (spot size <10 μm) with a photon energy of 6.3 eV [59]. The energy and angular resolutions were better than 3 meV and less than 0.05° (momentum resolution of 6×10^{-4} Å^{-1}), respectively [59]. A clean (001) sample surface was obtained *in situ* by cleaving crystals using the top-post method under ultrahigh vacuum with a pressure of 2.4×10^{-9} Pa and a temperature below 20 K.

Figure 1(a1) shows the ARPES result, exhibiting a Dirac-cone-like band dispersion of the TSS along the $\bar{\Gamma}-\bar{K}$ momentum direction at 17 K obtained from Bi_2Te_3 sample 1. The CB exists near the E_F at the $\bar{\Gamma}$ point, indicating that the present sample is an *n*-type semiconductor. The ARPES spectral features above the DP are more homogeneous and narrower for the $k_\parallel < 0$ side than for the $k_\parallel > 0$ side. The momentum-dependent photoemission intensity modulation is also visible in the Fermi surface map in Fig. 1(c). These results are likely due to the matrix element effect of the dipole transition, which depends on the experimental geometry and excitation photon energy [42]. Here, we examine the momentum distribution curves (MDCs) for the $k_\parallel < 0$ side and above

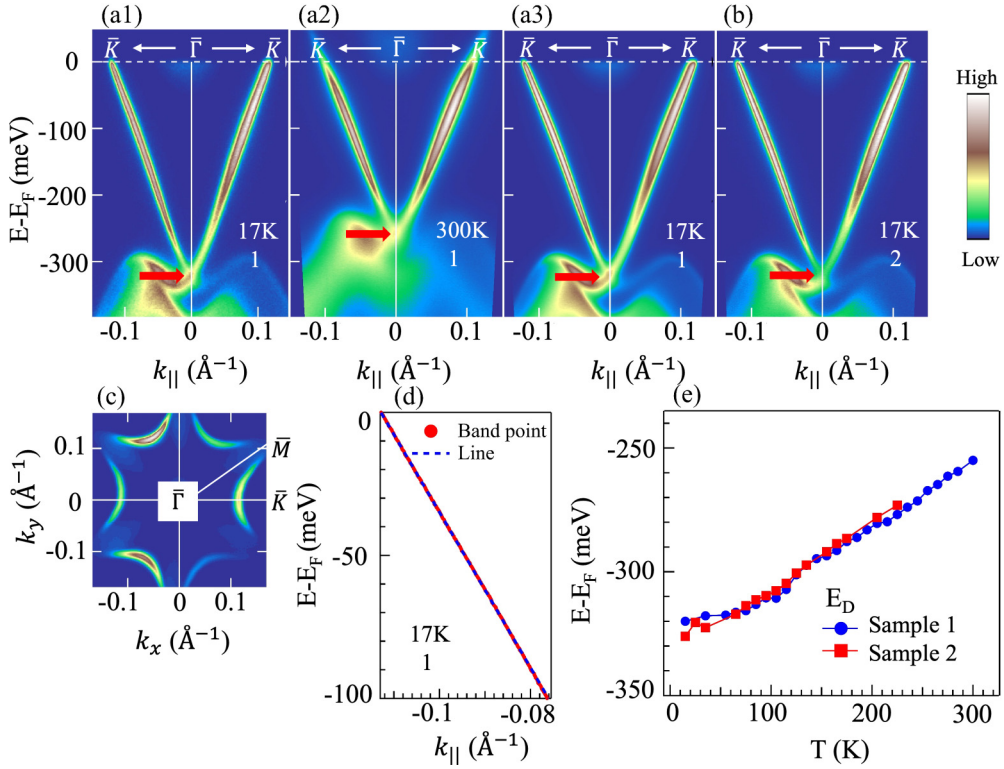

FIG. 1. ARPES intensity plots along $\bar{\Gamma} - \bar{K}$ of *n*-type Bi_2Te_3 sample 1 at 17 K (a1), 300 K (a2), and 17 K after the heating and cooling processes (a3). (b) ARPES intensity plot of Bi_2Te_3 sample 2 at 17 K. Red arrows in (a1)–(a3), and (b) indicate Dirac point (DP) position. (c) Observed Fermi surface of sample 1 measured at 17 K. (d) Band points evaluated near the E_F determined by the MDC analyses (red circles) of the data shown in (a1). To see the linearity, we plotted a dotted line (blue) connecting a band point at E_F and a band point at -100 meV. (e) Temperature-induced energy shift in the DP energy (E_D). The E_D of sample 1 was determined in the heating process from 17 to 300 K, and that of sample 2 was determined in the cooling process from 300 to 17 K.

the DP energy, and analyze the peak position by fitting to a Lorentzian function [60].

As the surface Debye temperature of Bi_2Te_3 was reported to be $\Theta_D = 81 \pm 6$ K ($\omega_D = k_B\Theta_D \sim 7$ meV) [30], the kink structure should exist within this energy range near E_F [61]. The solid red circles in Fig. 1(d) show the evaluated band points, which lie along the blue dashed line connecting two points, one at E_F and another at -100 meV. This indicates that there is no appreciable kink structure in the energy band dispersion at 17 K.

The DP energy (E_D) is 320 meV at 17 K [Fig. 1(a1)], and E_D is 255 meV at 300 K [Fig. 1(a2)], implying that the TSS carrier density decreases as the temperature increases [62,63]. We cool the sample to 17 K after 58 h of cleaving and obtain an ARPES spectrum, as shown in Fig. 1(a3). Even after the heating and cooling processes, the ARPES linewidth and E_D of ~321 meV at 17 K are highly reproducible. Furthermore, the ARPES spectrum at 17 K of sample 2, as shown in Fig. 1(b), exhibits $E_D \sim 327$ meV and the MDC peak widths that are almost identical to those of sample 1. Figure 1(e) shows that the temperature dependence of the E_D value during the heating of sample 1 and that during the cooling of sample 2 are almost the same, confirming the reproducibility of these observations [49,64].

Figure 2(a) shows the energy distribution curves (EDCs) of sample 1 at the $\bar{\Gamma}$ point at 17 and 300 K. The DP peak and the valence band (VB) peak are shifted upwards, i.e., closer to the E_F, as the temperature increases. Note that the peak separation between the DP and VB peaks was reduced from 79 meV at 17 K to 64 meV at 300 K. To examine the temperature dependence of the energy gap in the bulk, we analyze the EDCs and evaluate the energies for the VB peak (E_{VBP}) and conduction band bottom (E_{CBB}) positions at the $\bar{\Gamma}$ point [Fig. 2(b)]. Here E_{CBB} was determined by the zero-point crossing energy of the tangent line of the CB spectral feature. In Fig. 2(b), E_{VBP} increases as the temperature increases, while E_{CBB} is almost constant over temperature. Consequently, the energy difference $[\Delta E_1(T) = E_{CBB}(T) - E_{VBP}(T)]$ decreases as the temperature increases, as observed in other semiconductors [17,18]. The temperature-dependent energy shift or reduction in the band gap is formulated by

$$\Delta E(\vec{k}, \omega; T) = \int_0^{\omega_D} d\tilde{\omega}\alpha^2 F(\vec{k}, \omega; \tilde{\omega})\left[n(\tilde{\omega}, T) + \frac{1}{2}\right] \quad [17].$$

Note that at high temperatures where $k_BT \gg \omega + \omega_D$ or large electron excitation energies where $|\omega_D/\omega| \ll 1$, the right-hand side is proportional to $\frac{1}{\pi}|\mathrm{Im}\Sigma_{ep}(\vec{k}, \omega; T)|$ because we obtain the relation $f(\tilde{\omega} + \omega, T) + f(\tilde{\omega} - \omega, T) \sim 1$. Figure 2(c) shows the evaluated temperature dependence of the imaginary part of the self-energy at $|\vec{k}| = 0$ and $\omega = E_D$, $-\mathrm{Im}\Sigma_{ep}(|\vec{k}| = 0, \omega = E_D; T)$ [49]. To confirm the relation between the energy gap and the imaginary part of the self-energy at the $\bar{\Gamma}$ point, we plotted $\Delta E_1(T)$ as a function of

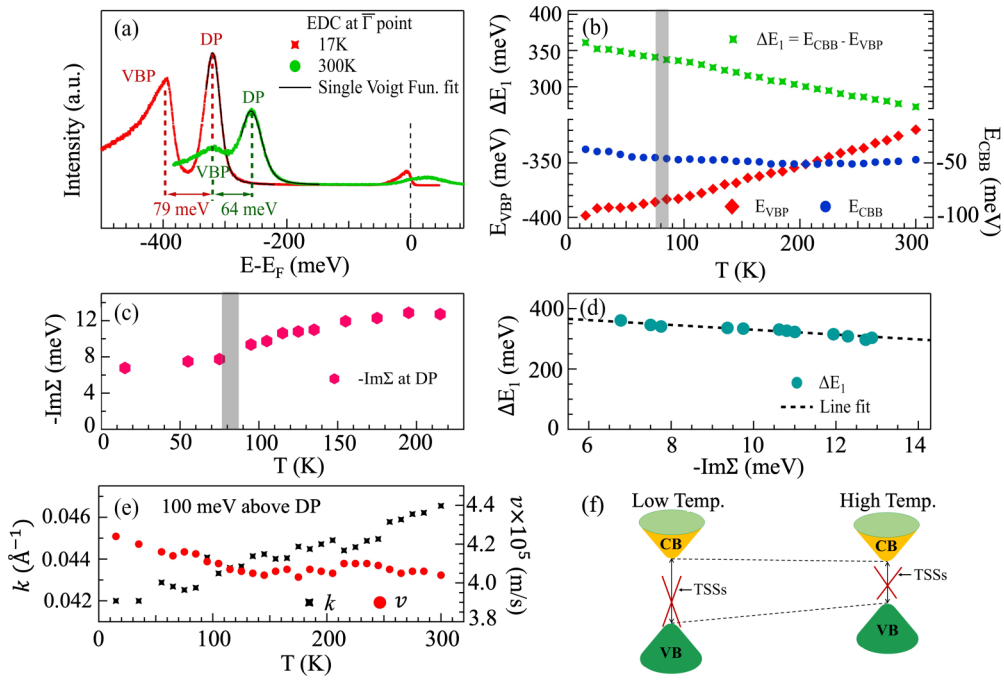

FIG. 2. (a) EDCs of sample 1 at the $\bar{\Gamma}$ point at 17 K (red) and 300 K (green). Solid black lines show the fitting results using a single Voigt function. (b) The lower panel depicts the energy position of the VB peak (E_{VBP}) and CB bottom (E_{CBB}). The upper panel shows the temperature dependence of the energy difference $\Delta E_1(T) = E_{\mathrm{CBB}}(T) - E_{\mathrm{VBP}}(T)$ at the $\bar{\Gamma}$ point. (c) Temperature-dependent $|\mathrm{Im}\Sigma(|\vec{k}| = 0, \omega = E_{\mathrm{D}}; T)|$ at the DP obtained from the EDC linewidth. The grey shaded areas in (b) and (c) show the reported surface Debye temperature, $\Theta_D = 81 \pm 6$ K ($\omega_D = k_B\Theta_D \sim 7$ meV) [30]. (d) Plot of $\Delta E_1(T)$ as a function of $-\mathrm{Im}\Sigma(0, E_{\mathrm{D}}; T)$ with a line fit. (e) Temperature dependence of the wave vector (k) and the group velocity (v) at a fixed energy (100 meV above the DP) on sample 1. (f) Schematic diagram of the temperature-dependent nonrigid-band-like band modification.

$-\mathrm{Im}\Sigma_{ep}(0, E_{\mathrm{D}}; T)$ in Fig. 2(d). One can clearly see a linear relation between these two quantities, indicating that the temperature dependence of the energy gap in the bulk is closely related to the self-energy due to the EPI. Note that the contribution of the EPI to the temperature dependence of the energy gap is larger than that of the thermal expansion [65]. Although the thermal expansion contribution is not negligible, these two contributions show similar temperature dependence at high temperatures [65].

Recently, Nayak *et al.* reported a similar temperature dependence in the TSS on Bi_2Te_2Se and explained this phenomenon through the temperature-dependent chemical potential shift, $\mu(T) = E_F - \frac{\pi^2}{6}\frac{D'(E_F)}{D(E_F)}(k_BT)^2$, where $E_F = \mu(T = 0)$ is the Fermi level, $D(E_F)$ is the DOS at the E_{F}, and $D'(E_F)$ is the gradient of the DOS at the E_{F} [66]. If the E_{F} is closer to the bottom of the CB, as in the present case, and the gradient of the DOS is positive, i.e., $D'(E_F) > 0$, then the chemical potential decreases as the temperature increases and the CB and VB peaks shift towards higher energy by the same amount. However, this is not what we observe in Fig. 2(b), indicating the significant role of the EPI.

As described above, the temperature-dependent band modification is obviously nonrigid-band like. Then, we examine the temperature dependence of the band dispersion of the TSS in more detail. In Fig. 2(e), we plot the temperature dependence of the wave number (k) and the group velocity (v) at the initial-state electron energy of 100 meV above the DP and along the $\bar{\Gamma}-\bar{K}$ momentum direction. Note that v is identical to the Fermi velocity v_F, as the linearity of the TSS band dispersion holds at each temperature. We can clearly see an increase in k and a decrease in v as the temperature increases. This indicates that the band dispersion of the TSS is compressed along the energy direction, as the energy gap in the bulk decreases as the temperature increases. Figure 2(f) shows a schematic diagram of the temperature-dependent nonrigid-band-like band modification observed in this study. Despite the nontrivial temperature-dependent band modification, we cannot detect any appreciable gap opening at the DP. Figure 2(a) shows the fitting results of the EDCs at 17 and 300 K using a single Voigt function. This confirms that the TSS is robust against bulk band modification derived from the EPI at finite temperatures, which is consistent with topological protection [3,4].

The upper panel of Fig. 3(a) shows the EPI coupling parameter $\lambda_{ep}(\omega')$ as a function of the initial-state electron energy measured from the DP energy ($\omega' = \omega - E_{\mathrm{D}}$; here, E_{D} is set to zero) along the $\bar{\Gamma}-\bar{K}$ momentum direction. The coupling parameters obtained from the MDC and EDC analyses agree well with each other. The EPI coupling parameter takes a maximum value of $\lambda_{ep} \sim 0.13$ at the DP ($\omega' = 0$), then decreases with increasing ω' and takes a minimum value of $\lambda_{ep} \sim 0.02$ at $\omega' \sim 100$ meV. Then, the coupling parameter slightly increases as the energy increases up to $\lambda_{ep} \sim 0.06$ at $\omega' = 250$ meV. Despite the temperature-dependent energy shift, when we evaluated the magnitude of the EPI coupling parameter at E_{F}, we obtained $\lambda_{ep} \sim 0.05$ [49]. For comparison, we plot the theoretical coupling parameters obtained from the first-principles calculations [41] in Fig. 3(a). The

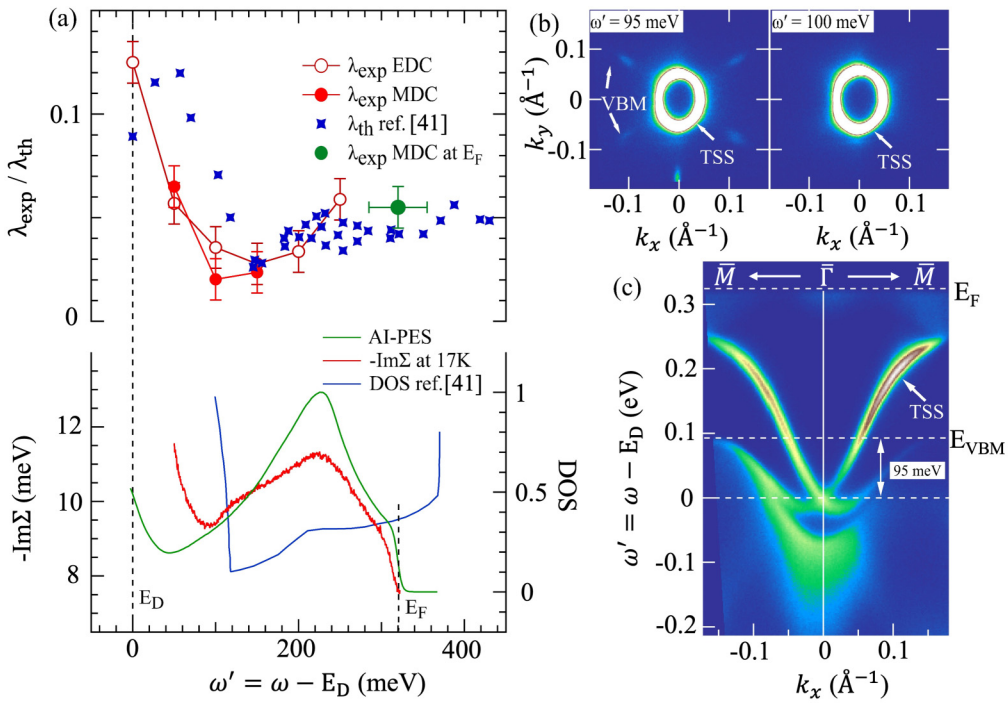

FIG. 3. (a) The upper panel shows the EPI coupling parameter as a function of initial-state electron energy with respect to the DP (ω') obtained from EDC analyses (open red circles) and MDC analyses (filled red circles). The filled green circle shows the EPI coupling parameter at E_F obtained from the MDC analyses, where the horizontal error represents the temperature-induced energy shift [49]. The blue stars represent the theoretical EPI coupling parameter extracted from Ref. [41]. The lower panel illustrates the experimental $-\mathrm{Im}\Sigma(\omega, T)$ at 17 K (red), theoretical DOS (blue), and angle-integrated photoemission spectrum (AI-PES in green). (b) Constant energy contours at 17 K showing the appearance (left, $\omega' = 95$ meV) and disappearance (right, $\omega' = 100$ meV) of the VBM. (c) ARPES intensity plot along $\bar{\Gamma}$-$\bar{M}$ at 17 K. Here we used sample 1.

theoretical EPI coupling parameter is $\lambda_{ep} \sim 0.1$ near the DP and reduces to $\lambda_{ep} \sim 0.03$ at 150 meV above E_D [41]. Note that the magnitude and the initial-state electron energy dependence of the coupling parameter of the experiments and the first-principles calculations agree well. Our results are also in line with a previous ARPES study, where $\lambda_{ep} \sim 0$ at 100 meV above DP (p-type Bi_2Te_3) [35].

First-principles calculations have revealed that the magnitude of the coupling parameter mainly depends on the number of scattering channels rather than the momentum dependence of the EPI matrix element [41]. Hence, the coupling parameter varies in accordance with the theoretical DOS, as shown in the lower panel of Fig. 3(a) [41]. To confirm this point, we show the imaginary part of the self-energy $-\mathrm{Im}\Sigma(\vec{k}, \omega'; T)$ obtained at 17 K [49] and the angle-integrated photoemission spectrum (AI-PES) in the lower panel of Fig. 3(a). Note that at a photon energy of $h\nu = 6.3$ eV, angle integration is performed only around the TSS over the momentum range of at most $\Delta k_{\parallel} \sim 0.34$ Å^{-1}. Therefore, the AI-PES mainly reflects the DOS derived from the TSS [67]. The energy dependence of the EPI coupling parameter coincides well with that of $-\mathrm{Im}\Sigma(\vec{k}, \omega'; T)$, which clearly indicates a correlation between $\lambda(\omega')$ and the scattering probability. If we compare $-\mathrm{Im}\Sigma(\vec{k}, \omega'; T)$ and the AI-PES, then the enhancement of $-\mathrm{Im}\Sigma(\vec{k}, \omega'; T)$ near the DP is more rapid, which suggests more scattering channels into the bulk band near the DP. The peak at $\omega' = 230$ meV in the AI-PES originates from the maximum of the TSS band along the $\bar{\Gamma}$–$\bar{M}$ momentum direction, as shown in Fig. 3(c). Therefore, the similarity of the TSS-derived AI-PES and $-\mathrm{Im}\Sigma(\vec{k}, \omega'; T)$ in the energy dependence at approximately $\omega' = 230$ meV indicates that the scattering channel is mainly restricted inside the TSS. The magnitude of the EPI coupling parameter and $-\mathrm{Im}\Sigma(\vec{k}, \omega'; T)$ reach the minimum at approximately 100 meV above the DP, where the valence band maximum (VBM) exists along the $\bar{\Gamma}$–$\bar{M}$ momentum direction, as seen in Fig. 3(b). Based on these theoretical results and our experimental results, the EPI coupling parameter in the TSS is weak, at most $\lambda_{ep} \sim 0.1$, which is consistent with the lack of an appreciable kink structure within the Debye energy range, as shown in Fig. 1(d) at 17 K. Our results indicate that EPI scattering can be minimized if we adjust the E_F position to approximately 100 meV above the DP in the case of Bi_2Te_3.

In conclusion, we examined the temperature-dependent band structures and energy dependence of the EPI of the TSS on n-type Bi_2Te_3 using high-resolution ARPES. We found that the temperature-dependent band modification was nonrigid-band like and that the EPI played a significant role at finite temperatures. Despite the temperature-dependent band modification in the bulk, the degeneracy at the DP was robust, showing topological protection. The EPI coupling parameter varied from 0.13 (at the DP) to 0.02 (100 meV above the DP),

which was consistent with the reported first-principles calculations. The imaginary part of the self-energy indicated that the EPI coupling parameter was determined by the number of scattering channels. Our results provided insight into the physical properties at finite temperatures originating from the TSS on 3D TIs.

The ARPES measurements were performed under Proposal No. 19BG053 and No. 20AU019 of the Hiroshima Synchrotron Radiation Center. We thank N-BARD, Hiroshima University, for supplying liquid helium. This work was supported by JSPS KAKENHI Grant No. 22K03495.

[1] C. L. Kane and E. J. Mele, Z_2 Topological Order and the Quantum Spin Hall Effect, Phys. Rev. Lett. **95**, 146802 (2005).

[2] L. Fu, C. L. Kane, and E. J. Mele, Topological Insulators in Three Dimensions, Phys. Rev. Lett. **98**, 106803 (2007).

[3] L. Fu and C. L. Kane, Topological insulators with inversion symmetry, Phys. Rev. B **76**, 045302 (2007).

[4] M. Z. Hasan and C. L. Kane, *Colloquium*: Topological insulators, Rev. Mod. Phys. **82**, 3045 (2010).

[5] X.-L. Qi and S.-C. Zhang, Topological insulators and superconductors, Rev. Mod. Phys. **83**, 1057 (2011).

[6] D. Hsieh, Y. Xia, D. Qian, L. Wray, J. H. Dil, F. Meier, J. Osterwalder, L. Patthey, J. G. Checkelsky, N. P. Ong, A. V. Fedorov, H. Lin, A. Bansil, D. Grauer, Y. S. Hor, R. J. Cava, and M. Z. Hasan, A tunable topological insulator in the spin helical Dirac transport regime, Nature (London) **460**, 1101 (2009).

[7] P. Roushan, J. Seo, C. V. Parker, Y. S. Hor, D. Hsieh, D. Qian, A. Richardella, M. Z. Hasan, R. J. Cava, and A. Yazdani, Topological surface states protected from backscattering by chiral spin texture, Nature (London) **460**, 1106 (2009).

[8] B. A. Bernevig, T. L. Hughes, and S. C. Zhang, Quantum spin Hall effect and topological phase transition in HgTe quantum wells, Science **314**, 1757 (2006).

[9] W. Z. Rui Yu, H.-J. Zhang, S.-C. Zhang, X. Dai, and Z. Fang, Quantized anomalous Hall effect in magnetic topological insulators, Science **329**, 61 (2010).

[10] L. Fu and C. L. Kane, Superconducting Proximity Effect and Majorana Fermions at the Surface of a Topological Insulator, Phys. Rev. Lett. **100**, 096407 (2008).

[11] L. A. Fu and E. Berg, Odd-Parity Topological Superconductors: Theory and Application to $Cu_xBi_2Se_3$, Phys. Rev. Lett. **105**, 097001 (2010); Y. S. Hor, A. J. Williams, J. G. Checkelsky, P. Roushan, J. Seo, Q. Xu, H. W. Zandbergen, A. Yazdani, N. P. Ong, and R. J. Cava, Superconductivity in $Cu_xBi_2Se_3$ and its Implications for Pairing in the Undoped Topological Insulator, *ibid.* **104**, 057001 (2010).

[12] X.-L. Qi, R. Li, J. Zang, and S.-C. Zhang, Inducing a magnetic monopole with topological surface states, Science **323**, 1184 (2009).

[13] D. Pesin and A. H. MacDonald, Spintronics and pseudospintronics in graphene and topological insulators, Nat. Mater. **11**, 409 (2012).

[14] P. Nozières, *Theory of Interacting Fermi Systems* (Addison-Wesley, Massachusetts, 1997).

[15] G. Grimvall, *The Electron-Phonon Interaction in Metals* (North-Holland, Amsterdam, 1981).

[16] G. D. Mahan, *Many-Particle Physics* (Kluwer Academic/Plenum, New York, 2000).

[17] P. B. Allen and M. Cardona, Theory of the temperature dependence of the direct gap of germanium, Phys. Rev. B **23**, 1495 (1981).

[18] T. P. O'Donnell and X. Chen, Temperature dependence of semiconductor band gaps, Appl. Phys. Lett. **58**, 2924 (1991).

[19] G. Antonius and S. G. Louie, Temperature-Induced Topological Phase Transisions: Promoted Versus Suppressed Nontrivial Topology, Phys. Rev. Lett. **117**, 246401 (2016); T. Imai, J. Chen, K. Kato, K. Kuroda, T. Matsuda, A. Kimura, K. Miyamoto, S. V. Eremeev, and T. Okuda, Experimental verification of a temperature-induced topological phase transition in $TlBiS_2$ and $TlBiSe_2$, Phys. Rev. B **102**, 125151 (2020).

[20] H. Wang, Y. Pei, A. D. LaLonde, and G. J. Snyder, Weak electron–phonon coupling contributing to high thermoelectric performance in *n*-type PbSe, Proc. Natl. Acad. Sci. USA **109**, 9705 (2012); M. Wiesner, A. Trzaskowska, B. Mroz, S. Charpentier, S. Wang, Y. Song, F. Lombardi, P. Lucignano, G. Benedek, D. Campi, M. Bernasconi, F. Guinea, and A. Tagliacozzo, The electron-phonon interaction at deep Bi_2Te_3-semiconductor interfaces from Brillouin light scattering, Sci. Rep. **7**, 16449 (2017).

[21] Z. Liu, X. Yao, J. Shao, M. Zuo, L. Pi, S. Tan, C. Zhang, and Y. Zhang, Superconductivity with topological surface state in $Sr_xBi_2Se_3$, J. Am. Chem. Soc. **137**, 10512 (2015); Shruti, V. K. Maurya, P. Neha, P. Srivastava, and S. Patnaik, Superconductivity by Sr intercalation in the layered topological insulator Bi_2Se_3, Phys. Rev. B **92**, 020506(R) (2015).

[22] K. Kobayashi, T. Ueno, H. Fujiwara, T. Yokoya, and J. Akimitsu, Unusual upper critical field behavior in Nb-doped bismuth selenides, Phys. Rev. B **95**, 180503(R) (2017).

[23] D. Kim, Q. Li, P. Syers, N. P. Butch, J. Paglione, S. Das Sarma, and M. S. Fuhrer, Intrinsic Electron-Phonon Resistivity of Bi_2Se_3 in the Topological Regime, Phys. Rev. Lett. **109**, 166801 (2012).

[24] M. V. Costache, I. Neumann, J. F. Sierra, V. Marinova, M. M. Gospodinov, S. Roche, and S. O. Valenzuela, Fingerprints of Inelastic Transport at the Surface of the Topological Insulator Bi_2Se_3: Role of Electron-Phonon Coupling, Phys. Rev. Lett. **112**, 086601(2014).

[25] X. Zhu, L. Santos, R. Sankar, S. Chikara, C. Howard, F. C. Chou, C. Chamon, and M. El-Batanouny, Interaction of Phonons and Dirac Fermions on the Surface of Bi_2Se_3: A Strong Kohn Anomaly, Phys. Rev. Lett. **107**, 186102 (2011).

[26] X. Zhu, L. Santos, C. Howard, R. Sankar, F. C. Chou, C. Chamon, and M. El-Batanouny, Electron-Phonon Coupling on the Surface of the Topological Insulator Bi_2Se_3 Determined from Surface-Phonon Dispersion Measurements, Phys. Rev. Lett. **108**, 185501 (2012).

[27] C. Howard and M. El-Batanouny, Connecting electron and phonon spectroscopy data to consistently determine quasiparticle-phonon coupling on the surface of topological insulators, Phys. Rev. B **89**, 075425 (2014).

[28] C. Howard, M. El-Batanouny, R. Sankar, and F. C. Chou, Anomalous behavior in the phonon dispersion of the (001) surface of Bi_2Te_3 determined from helium atom-surface scattering measurements, Phys. Rev. B **88**, 035402 (2013).

[29] A. Ruckhofer, D. Campi, M. Bremholm, P. Hofmann, G. Benedek, M. Bernasconi, W. E. Ernst, and A. Tamtögl, Terahertz surface modes and electron-phonon coupling on Bi_2Se_3(111), Phys. Rev. Research **2**, 023186 (2020).

[30] A. Tamtoegl, P. Kraus, N. Avidor, M. Bremholm, E. M. J. Hedegaard, B. B. Iversen, M. Bianchi, P. Hofmann, J. Ellis, W. Allison, G. Benedek, and W. E. Ernst, Electron-phonon coupling and surface debye temperature of Bi_2Te_3(111) from helium atom scattering, Phys. Rev. B **95**, 195401 (2017).

[31] R. C. Hatch, M. Bianchi, D. Guan, S. Bao, J. Mi, B. B. Iversen, L. Nilsson, L. Hornekær, and P. Hofmann, Stability of the Bi_2Se_3(111) topological state: Electron-phonon and electron-defect scattering, Phys. Rev. B **83**, 241303(R) (2011).

[32] Z. H. Pan, A. V. Fedorov, D. Gardner, Y. S. Lee, S. Chu, and T. Valla, Measurement of an Exceptionally Weak Electron-Phonon Coupling on the Surface of the Topological Insulator Bi_2Se_3 Using Angle-Resolved Photoemission Spectroscopy, Phys. Rev. Lett. **108**, 187001 (2012).

[33] J. Sánchez-Barriga, M. R. Scholz, E. Golias, E. Rienks, D. Marchenko, A. Varykhalov, L. V. Yashina, and O. Rader, Anisotropic effect of warping on the lifetime broadening of topological surface states in angle-resolved photoemission from Bi_2Te_3, Phys. Rev. B **90**, 195413 (2014).

[34] T. Kondo, Y. Nakashima, Y. Ota, Y. Ishida, W. Malaeb, K. Okazaki, S. Shin, M. Kriener, S. Sasaki, K. Segawa, and Y. Ando, Anomalous Dressing of Dirac Fermions in the Topological Surface State of Bi_2Se_3, Bi_2Te_3, and Cu-Doped Bi_2Se_3, Phys. Rev. Lett. **110**, 217601 (2013).

[35] C. Chen, Z. Xie, Y. Feng, H. Yi, A. Liang, S. He, D. Mou, J. He, Y. Peng, X. Liu, Y. Liu, L. Zhao, G. Liu, X. Dong, J. Zhang, L. Yu, X. Wang, Q. Peng, Z. Wang, S. Zhang *et al.*, Tunable Dirac fermion dynamics in topological insulators, Sci. Rep. **3**, 2411 (2013).

[36] S. Giraud and R. Egger, Electron-phonon scattering in topological insulators, Phys. Rev. B **83**, 245322 (2011).

[37] S. Giraud, A. Kundu, and R. Egger, Electron-phonon scattering in topological insulator thin films, Phys. Rev. B **85**, 035441 (2012).

[38] S. Das Sarma and Q. Li, Many-body effects and possible superconductivity in the two-dimensional metallic surface states of three-dimensional topological insulators, Phys. Rev. B **88**, 081404(R) (2013).

[39] V. Parente, A. Tagliacozzo, F. von Oppen, and F. Guinea, Electron-phonon interaction on the surface of a three-dimensional topological insulator, Phys. Rev. B **88**, 075432 (2013).

[40] G. Q. Huang, Surface lattice vibration and electron-phonon interaction in topological insulator Bi_2Te_3(111) films from first principles, Europhys. Lett. **100**, 17001 (2012).

[41] R. Heid, I. Y. Sklyadneva, and E. V. Chulkov, Electron-phonon coupling in topological surface states: the role of polar optical modes, Sci. Rep. **7**, 1095 (2017).

[42] A. Damascelli, Z. Hussain, and Z. X. Shen, Angle-resolved photoemission studies of the cuprate superconductors, Rev. Mod. Phys. **75**, 473 (2003).

[43] E. W. Plummer, J. Shi, S.-J. Tang, E. Rotenberg, and S. D. Kevan, Enhanced electron–phonon coupling at metal surfaces, Prog. Surf. Sci. **74**, 251 (2003).

[44] P. Hofmann, I. Y. Sklyadneva, E. D. L. Rienks, and E. V. Chulkov, Electron–phonon coupling at surfaces and interfaces, New J. Phys. **11**, 125005 (2009).

[45] S. Raghu, S. B. Chung, X.-L. Qi, and S.-C. Zhang, Collective modes of a helical liquid, Phys. Rev. Lett. **104**, 116401 (2010).

[46] J. Jiang, K. Shimada, H. Hayashi, H. Iwasawa, Y. Aiura, H. Namatame, and M. Taniguchi, Coupling parameters of many-body interactions for the Al(100) surface state: a high-resolution angle-resolved photoemission spectroscopy study, Phys. Rev. B **84**, 155124 (2011).

[47] B. K. Gupta, R. Sultana, S. Singh, V. Singh, G. Awana, A. Gupta, B. Singh, A. K. Srivastava, O. N. Srivastava, S. Auluck, and V. P. S. Awana, Unexplored photoluminescence from bulk and mechanically exfoliated few layers of Bi_2Te_3, Sci. Rep. **8**, 9205 (2018).

[48] A. Singh, R. Singh, T. Patel, G. S. Okram, A. Lakhani, V. Ganeshan, A. K. Ghosh, S. N. Jha, S. Patil, and S. Chatterjee, Tuning of carrier type, enhancement of linear magnetoresistance and inducing ferromagnetism at room temperature with Cu doping in Bi_2Te_3 topological insulators, Mater. Res. Bull. **98**, 1 (2018).

[49] See Supplemental Material at http://link.aps.org/supplemental/10.1103/PhysRevB.106.L121104 for more details, which includes Refs. [50–58].

[50] P. D. C. King, R. C. Hatch, M. Bianchi, R. Ovsyannikov, C. Lupulescu, G. Landolt, B. Slomski, J. H. Dil, D. Guan, J. L. Mi, E. D. L. Rienks, J. Fink, A. Lindblad, S. Svensson, S. Bao, G. Balakrishnan, B. B. Iversen, J. Osterwalder, W. Eberhardt, F. Baumberger, and P. Hofmann, Large Tunable Rashba Spin Splitting of a Two-Dimensional Electron Gas in Bi_2Se_3, Phys. Rev. Lett. **107**, 096802 (2011).

[51] K. Sakamoto, H. Ishikawa, T. Wake, C. Ishimoto, J. Fujii, H. Bentmann, M. Ohtaka, K. Kuroda, N. Inoue, T. Hattori, T. Miyamachi, F. Komori, I. Yamamoto, C. Fan, P. Kruger, H. Ota, F. Matsui, F. Reinert, J. Avila, and M. C. Asensio, Spatial control of charge doping in n-Type topological insulators, Nano Lett. **21**, 4415 (2021).

[52] M. S. Bahramy, P. D. C. King, A. de la Torre, J. Chang, M. Shi, L. Patthey, G. Balakrishnan, P. Hofmann, R. Arita, N. Nagaosa, and F. Baumberger, Emergent quantum confinement at topological insulator surfaces, Nat. Commun. **3**, 1159 (2012).

[53] Z. H. Zhu, G. Levy, B. Ludbrook, C. N. Veenstra, J. A. Rosen, R. Comin, D. Wong, P. Dosanjh, A. Ubaldini, P. Syers, N. P. Butch, J. Paglione, I. S. Elfimov, and A. Damascelli, Rashba Spin-Splitting Control at the Surface of the Topological Insulator Bi_2Se_3, Phys. Rev. Lett. **107**, 186405 (2011).

[54] E. Frantzeskakis, N. De Jong, B. Zwartsenberg, Y. K. Huang, T. V. Bay, P. Pronk, E. Van Heumen, D. Wu, Y. Pan, M. Radovic, N. C. Plumb, N. Xu, M. Shi, A. De Visser, and M. S. Golden, Micro-metric electronic patterning of a topological band structure using a photon beam, Sci. Rep. **5**, 16309 (2015).

[55] E. Frantzeskakis, S. V. Ramankutty, N. de Jong, Y. K. Huang, Y. Pan, A. Tytarenko, M. Radovic, N. C. Plumb, M. Shi, A. Varykhalov, A. de Visser, E. van Heumen, and M. S. Golden, Trigger of the Ubiquitous Surface Band Bending in 3D Topological Insulators, Phys. Rev. X **7**, 041041 (2017).

[56] A. A. Kordyuk, T. K. Kim, V. B. Zabolotnyy, D. V. Evtushinsky, M. Bauch, C. Hess, B. Buchner, H. Berger, and S. V. Borisenko, Photoemission-induced gating of topological insulators, Phys. Rev. B **83**, 081303(R) (2011).

[57] M. S. Hofman, D. Z. Wang, Y. Yang, and B. E. Koel, Interactions of incident H atoms with metal surfaces, Surf. Sci. Rep. **73**, 153 (2018).

[58] R. A. Ciufo, S. M. Han, M. E. Floto, J. E. Eichler, G. Henkelman, and C. B. Mullins, Hydrogen desorption from the surface and subsurface of cobalt, Phys. Chem. Chem. Phys. **22**, 15281 (2020).

[59] H. Iwasawa, E. F. Schwier, M. Arita, A. Ino, H. Namatame, M. Taniguchi, Y. Aiura, and K. Shimada, Development of laser-based scanning μ-ARPES system with ultimate energy and momentum resolutions, Ultramicroscopy **182**, 85 (2017).

[60] The contribution from the instrumental momentum resolution to the linewidth is negligible [59].

[61] N. W. Ashcroft and N. D. Mermin, *Solid State Physics* (Sanders College, Philadelphia, 1976), Chap. 26.

[62] R. Jiang, L. L. Wang, M. L. Huang, R. S. Dhaka, D. D. Johnson, T. A. Lograsso, and A. Kaminski, Reversible tuning of the surface state in a pseudobinary $Bi_2(Te\text{-}Se)_3$ topological insulator, Phys. Rev. B **86**, 085112 (2012).

[63] E. Frantzeskakis, N. de Jong, B. Zwartsenberg, T. V. Bay, Y. K. Huang, S. V. Ramankutty, A. Tytarenko, D. Wu, Y. Pan, S. Hollanders, M. Radovic, N. C. Plumb, N. Xu, M. Shi, C. Lupulescu, T. Arion, R. Ovsyannikov, A. Varykhalov, W. Eberhardt, A. de Visser *et al.*, Dirac states with knobs on: Interplay of external parameters and the surface electronic properties of three-dimensional topological insulators, Phys. Rev. B **91**, 205134 (2015).

[64] We have investigated the surface degradation and photon irradiation effects on the TSS using our ARPES system; see D. A. Estyunin, E. F. Schwier, S. Kumar, K. Shimada, K. Kokh, O. E. Tereshchenko, and A. M. Shikin, Features and applications of the energy shift of the topological surface state, Phys. Rev. B **105**, 125303 (2022).

[65] B. Monserrat and D. Vanderbilt, Temperature Effects in the Band Structure of Topological Insulators, Phys. Rev. Lett. **117**, 226801 (2016).

[66] J. Nayak, G. H. Fecher, S. Ouardi, C. Shekhar, C. Tusche, S. Ueda, E. Ikenaga, and C. Felser, Temperature-induced modification of the Dirac cone in the tetradymite topological insulator Bi_2Te_2Se, Phys. Rev. B **98**, 075206 (2018).

[67] As we only used a single photon energy of 6.3 eV in the experiments, the angle integration along the k_z direction for the bulk-derived band is rather limited, which suppresses the bulk contribution to the AI-PES, especially near the DP. If we use higher photon energies, we may achieve an AI-PES closer to the theoretical DOS [see, e.g., Z. Alpichshev, J. G. Analytis, J. H. Chu, I. R. Fisher, Y. L. Chen, Z. X. Shen, A. Fang, and A. Kapitulnik, STM Imaging of Electronic Waves on the Surface of Bi_2Te_3: Topologically Protected Surface States and Hexagonal Warping Effects, Phys. Rev. Lett. **104**, 016401 (2010); Y. L. Chen, J. G. Analytis, J.-H. Chu, Z. K. Liu, S.-K. Mo, X. L. Qi, H. J. Zhang, D. H. Lu, X. Dai, Z. Fang, S. C. Zhang, I. R. Fisher, Z. Hussain, and Z.-X. Shen, Experimental realization of a three-dimensional topological insulator, Bi_2Te_3, Science **325**, 178 (2009)].